THE JOURNAL OF PHYSICAL CHEMISTRY C

Article

pubs.acs.org/JPCC

Modeling of Unidirectional-Overloaded Transition in Catalytic Tubular Microjets

Anke Klingner,[†] Islam S. M. Khalil,[*,‡] Veronika Magdanz,[§] Vladimir M. Fomin,[§] Oliver G. Schmidt,[§,∥] and Sarthak Misra[⊥,#]

[†]Department of Physics and [‡]Department of Mechatronics, The German University in Cairo, Cairo 11432, Egypt

[§]Institute for Integrative Nanosciences, IFW Dresden, D-01069 Dresden, Germany

[∥]University of Technology Chemnitz, 09111 Chemnitz, Germany

[⊥]Department of Biomechanical Engineering, University of Twente, 7522 NB Enschede, The Netherlands

[#]Department of Biomedical Engineering, University of Gronignen and University Medical Center Gronignen, 9713 GZ Groningen, The Netherlands

Supporting Information

ABSTRACT: A numerical time-resolved model is presented for predicting the transition between unidirectional and overloaded motion of catalytic tubular microjets (Ti/Fe/Pt rolled-up microtubes) in an aqueous solution of hydrogen peroxide. Unidirectional movement is achieved by periodic ejection of gas bubbles from one end, whereas formation of multiple bubbles hinders microjet movement in overloaded regime. The influence of nucleation positions of bubbles, hydrogen peroxide concentration, liquid-platinum contact angle, microjet length, and cone angle on the bubble ejection frequency and microjet speed are investigated. We find agreement between the theoretical speeds of the microjet for a range of bubble nucleation positions ($0.4L \leq x_0 \leq 0.6L$) and our measurements (108 ± 35 μm/s) for unidirectional motion. In addition, we observe experimentally that transition to overloaded motion occurs for hydrogen peroxide concentration of 5%, whereas our model predicts this transition for concentrations above 2.5%.

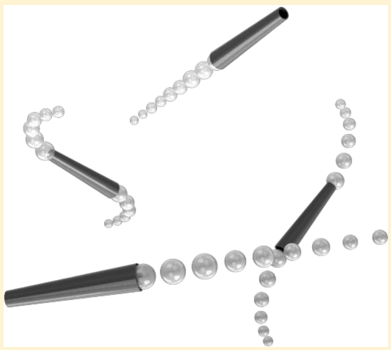

1. INTRODUCTION

Over the past decade, external actuation of man-made robots[1−7] at the nano- and microscales has shown potential to revolutionize medicine and technology.[8−11] It is possible to direct and/or drive these robots via the action of a magnetic field without the need of onboard power supply and control system. One of the simplest designs for man-made robots at the nano- and microscale consists of a catalytic self-driving mechanism,[12−20] which utilizes the chemical energy resulting from the catalytic reaction between the robot surface and the surrounding medium to provide propulsion. In this approach the navigation relies only on a dynamic magnetic fields,[21−23] allowing for simple motion control and accurate localization in two-[24,25] and three-dimensional[26] spaces. Several mathematical models of various types[27−29] of self-driving mechanisms have been proposed to study and optimize the locomotion. Favelukis et al. have presented a model for momentum- and mass-transfer-controlled spherical bubble growth and showed that the driving force for mass transfer increases as the reaction rate increases. In addition, this model predicts that the growth rate of the bubble increases owing to a decrease in the surface concentration.[30] Manjare et al. have formulated one-dimensional reaction diffusion equations to describe the mass transport and reaction in a cylindrical microjet.[31] These diffusion equations predict the consumption rates and distribution of hydrogen peroxide and oxygen only at one end of the microjet. Li et al. have proposed a simple model to predict the average speed of the microjet based on the product of the bubble radius and bubble ejection frequency.[32] However, this model is based on the assumption that the microjet has an ideal cylindrical shape, while typical tubular micromotors are asymmetric. A hydrodynamic model considering both the bubble geometry and buoyancy force has been proposed by Li et al. to identify the mechanism of a self-propelled conical tubular micromotor in an aqueous solution of hydrogen peroxide.[33] In addition, Fomin et al. have considered the geometric asymmetry and modeled the propulsion force of the microjets based on the development of a capillary force owing to the growth of the bubble in an asymmetrical tube.[34] The dependence of motility of microjets on the concentration of surfactants (required for detachment of the bubble from the microjet) and type (anionic, cationic, and neutral surfactants) has been studied by Wang et al.[35] They have observed that micorjets are more active in the presence of anionic surfactant than nonionic and cationic surfactants. A unified solution of the drag force and drag coefficient for all circular cross-sectional types of microjets has been presented.[36] This model provides a useful tool to optimize

Received: March 15, 2017
Revised: May 24, 2017
Published: June 1, 2017

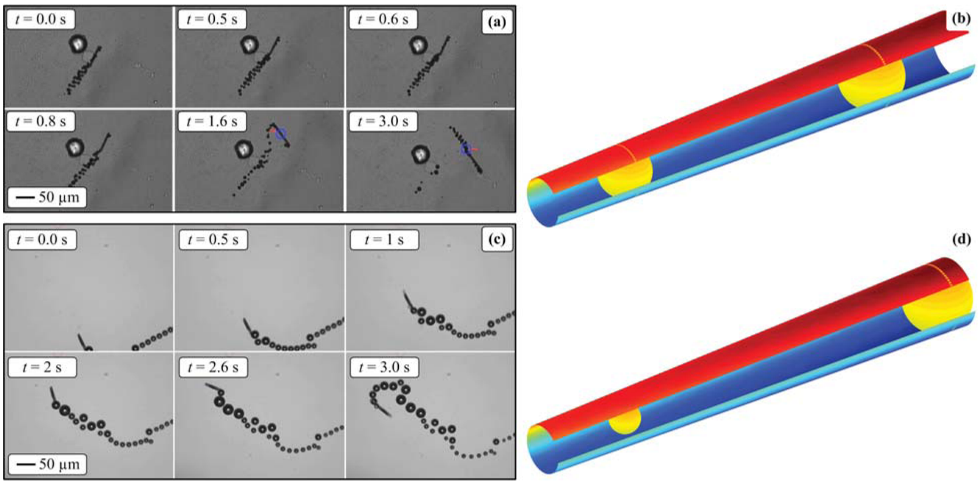

Figure 1. Ejection of oxygen bubbles by the catalytic decomposition of hydrogen peroxide fuel results in self-propulsive force and locomotion in low Reynolds number fluids. (a) Bubble ejection at both microjet ends in overloaded regime results in negligible net displacement of the microjet. (b) Simulation of a microjet in the overloaded regime. (c) The microjet moves at an average speed of two body lengths per second in the unidirectional regime with bubble ejection from the wider microjet end. (d) Simulation of a microjet in the unidirectional regime.

the parameters of the microjet. In addition, the near-surface effects of a channel or vascular network (hydrogen peroxide is available in blood[38] at concentration of 2×10^{-10} mol/L) on the propulsion of self-propelled microjet have been investigated theoretically by Sarkis et al.[37] It follows from the mentioned theoretical models that the existing experimental work has been partially explained, but several discrepancies between the actual model of the microjet and theory still exist. For instance, the influence of microjet parameters and hydrogen peroxide concentration on the nucleation of multiple bubbles and transition between unidirectional and overloaded motion has not yet been addressed. Here, we study the influence of multiple oxygen bubbles on the motion of microjets during transition from unidirectional microjet movement to overloaded flow, and we expand on the work of Manjare et al.,[31] Li et al.,[32] and Fomin et al.[34]

Catalytic tubular microjets are made of Ti/Fe/Pt rolled-up microtubes. The catalytic microjets have length of 50 μm and are prepared with a composition of the nanomembranes of Ti (5 nm), Fe (5 nm) and Pt (3 nm). The fabrication process is based on rolled up technology.[15] The inner surface of the microjet is coated with platinum, and the microjet is immersed in a hydrogen peroxide (H_2O_2) solution. The following chemical reaction produces oxygen upon contact between the platinum and the hydrogen peroxide fuel:

$$2H_2O_2 \rightarrow 2H_2O + O_2 \tag{1}$$

The conical shape of the microjet enables oxygen bubbles to be ejected from the wider end thus providing unidirectional propulsion, as shown in Figure 1. In the overloaded regime, bubbles are ejected from both microjet ends and reduce its speed to approximately zero, as shown in Figure 1a,b.[32] In this work, we develop a numerical time-resolved model to describe hydrogen peroxide decomposition and oxygen formation, oxygen and hydrogen peroxide diffusion, multiple bubbles nucleation and growth, bubble movement and ejection, and microjet movement. The extension with nucleation of multiple bubbles allows us to differentiate between unidirectional (Figure 1c,d)) microjet movement and overloaded microjets. This modification enables a correct selection of microjet parameters to avoid operating in overloaded regimes.

The remainder of this paper is organized as follows: Section 2 provides modeling of the microjet using multiple bubbles nucleation. The results of this model are included in Section 3. Discussions pertaining to differences between the existing models in the literature and the model presented in this study are provided in Section 4. Finally, Section 5 concludes and provides directions for future work.

2. MULTIPLE BUBBLES NUCLEATION MODEL

A microjet has an average radius, $r = \frac{r_{\min} + r_{\max}}{2}$, where $r_{\min}$ and $r_{\max}$ are the small and large radii of the microjet, respectively (Figure 2a). The microjet has a conical geometry of length L and angle ϕ obtained using $\phi = \tan^{-1}\left(\frac{r_{\max} - r_{\min}}{L}\right)$. It is aligned along the x-axis in the range, $0 \le x \le L$, so that the jet radius function ($r_j(x)$) is given by

$$r_j(x) = r_{\min} + x \tan \phi \tag{2}$$

Oxygen bubbles nucleate at position x_0 and time t_i, where i indicates the bubble number (Figure 2b). Therefore, the initial bubble volume, position, and nucleation time of the first bubble are $V_i(t_i) = 0$, $x_i(t_i) = x_0$, and $t_1 = 0$ s, respectively. Bubbles grow by collecting oxygen as they move inside the microjet. Therefore, the model of the microjet is based on the rate of change of bubble volume ($V_i(t)$) and the bubble position ($x_i(t)$), until the final time (t_f). The final time and microjet movement regime (n) are determined by the occurrence of bubble ejection ($n = 1$) or blockage of the microjet with several bubbles ($n \ge 2$), and is described using

$$(t, n) = \begin{cases} (t_f, 1) & \text{for } x_1(t) > L + \sqrt{\left(\frac{3V_1(t)}{4\pi}\right)^{2/3} - r_{\max}^2}, \\ (t_f, 2) & \text{for } V_2(t) \ge \frac{4}{3}\pi r_j^3(x_2), \\ (t, 3) & \text{otherwise} \end{cases} \tag{3}$$

For each set of parameters, the numerical time-resolved model continues until, $t = t_f$. Then, microjet behavior is classified as unidirectional or overloaded according to Table 1. Ejection

DOI: 10.1021/acs.jpcc.7b02447
J. Phys. Chem. C 2017, 121, 14854−14863

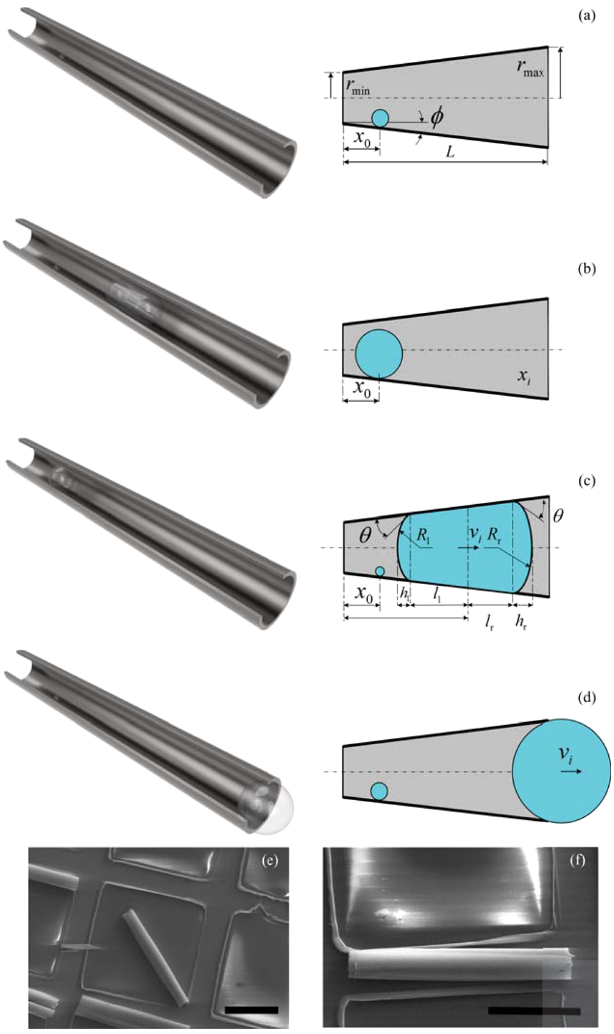

Figure 2. Schematic representation of a catalytic tubular microjet. (a) The microjet has length L, minimum radius r_{min}, maximum radius r_{max}, conical angle ϕ, liquid-platinum contact angle θ. (b) The first bubble nucleates and grows at position x_0. (c,d) The second bubble nucleates and grows at position x_0. The first bubble moves at speed v_i toward the wider microjet end with ejection frequency f and radius r_e, to initiate unidirectional microjet motion along the opposite direction. The bubble shape is geometrically described by two spherical caps (left and right) of radii R_l and R_r, and heights h_l and h_r and two cones of length l_l and l_r. (e) Ti/Fe/Pt rolled-up microtubes. Scale bar is 25 μm. (f) The jet is prepared with a composition of the nanomembranes of Ti (5 nm), Fe (5 nm), and Pt (3 nm). Scale bar is 25 μm. (e) and (f) are scanning electron microscopy images of the rolled up microjets.

frequency f, radius of ejected bubble r_e, and average bubble speed ($\overline{v}_b$) are evaluated and analyzed.

2.1. Time-Dependence of Bubble Volume. The time-dependence of the bubble volume $V_i(t)$ is based on catalytic formation of oxygen and its diffusion. The catalytically formed oxygen (with volume $V_0(x, t)$) after a time step Δt and its diffusion are governed by[31]

$$V_o(x, t + \Delta t) = V_o(x, t) + K_o c_H(x, t) A(x) \Delta t + \frac{D_o}{\Delta x^2} \Delta t (V_o(x - \Delta x, t) - 2V_o(x, t) + V_o(x + \Delta x, t)) \quad (4)$$

where K_0, $c_H(x, t)$, and D_0 are the rate constant of oxygen production, local hydrogen peroxide concentration, and oxygen diffusion constant, respectively. This volume is calculated at discrete positions separated by small increments Δx, where $\Delta x = L/N$, and N is the number of segments along the microjet. Linearization of diffusion law is justified as the time step is set to $\Delta t = \frac{\Delta x^2}{10 D_0}$, so that the prefactor of diffusion term is 1/10. The catalytically active local surface has an inner cylindrical area $A(x) = 2\pi r_j(x)\Delta x$, where Δx is the local increment along the x-axis and $r_j(x)$ is the microjet radius at position x. The initial condition is $V_0(x,0) = 0$. Hydrogen peroxide consumption and diffusion are governed by the following equation:

Table 1. Parameters of the unidirectional and overloaded regimes. The ejection frequency is denoted by f, radius of ejected bubble is r_e, average bubble speed is $\overline{v}_b$, and average microjet speed is $\overline{v}_j$ for the two regimes of microjet movement

microjet motion	unidirectional	overloaded
n	1	2
f	$\frac{1}{t_f}$	0
r_e	$\left[\frac{3V_i(t_f)}{4\pi}\right]^{1/3}$	0
$\overline{v}_b$	$\frac{x_1(t_f) - x_0}{t_f}$	0
$\overline{v}_j$	$\frac{1}{t_f}\int_0^{t_f} v_j \, dt$	0

$$c_H(x, t + \Delta t) = c_H(x, t) - \frac{2K_H}{r_j(x)} c_H(x, t)\Delta t + \frac{D_H}{\Delta x^2}\Delta t(c_H(x - \Delta x, t) - 2c_H(x, t) + c_H(x + \Delta x, t)) \quad (5)$$

where K_H and D_H are the rate and diffusion constants of the hydrogen peroxide solution, respectively. The initial condition is, $c_H(x,0) = c_0$. Now, bubble volume $V_i(t)$ grows by collecting oxygen with volume $V_0(x, t)$ along the bubble length from minimum bubble position (x_{min}) to maximum bubble position (x_{max}) according to

$$V_i(t + \Delta t) = V_i(t) + \sum_{x=x_{min}}^{x_{max}} V_o(x, t + \Delta t) \quad (6)$$

We apply the condition of oxygen balance, $V_0(x_{min} \leq x \leq x_{max}, t + \Delta t) = 0$. Minimum and maximum bubble positions are determined from the bubble geometry. The bubble is divided into two equal volumes V_l and V_r located left and right with respect to bubble position x_i, respectively ($V_l = V_r = V_i/2$). Each of these volumes consists of a cone of length l and a spherical cap of height h (Figure 2c). The cone volume is calculated using

$$V_c = \frac{\pi l}{3}(r_j^2(x_i) + r_j^2(x_i \pm l) + r_j(x_i) r_j(x_i \pm l)) \quad (7)$$

where $\pm$ is for the right and left cones, respectively. Further, the volume of the spherical cap (V_s) is given by

$$V_s = \frac{\pi h}{3}(3r_j(x_i \pm l)^2 + h^2) \quad (8)$$

If the bubble ends inside the microjet, the spherical cap forms contact angle θ with the wall of the microjet. Using x_{min} = max $(0, x_i - l_l - h_l)$ and x_{max} = min $(L, x_i + l_r + h_r)$, the hydrogen peroxide concentration is set to zero in the cone range $c_H(x_i - l_l \leq x \leq x_i + l_r, t + \Delta t) = 0$ (platinum surface is in contact with oxygen in this region).

DOI: 10.1021/acs.jpcc.7b02447
J. Phys. Chem. C 2017, 121, 14854−14863

2.2. Time-Dependence of Bubble Position. The bubble position $x_1(t)$ is determined using, $x_1(t+\Delta t) = x_1(t) + v_b(t)\,\Delta t$, where $v_b(t)$ is the time-dependent bubble speed. The bubble speed results in a change of the bubble position and movement of hydrogen peroxide solution, $c_H(x,t) = c_H(x - v_i\,\Delta t,t)$. Bubble $i + 1$ nucleates if bubble i is relatively far from nucleation position x_0 ($x_i > x_0 + l_l + h_l$). The relative speed ($v_b(t)$) of the bubble with respect to microjet wall is calculated by[42]

$$v_b(t) = 0.012\pi F_p \frac{r_j^2(x_i)}{\eta V_i(t)} \tag{9}$$

where η is the dynamic viscosity of the medium. Further, F_p is a force due to the pressure difference between the left and right spherical caps of the bubble,[41] and it is given by

$$F_p = \pi r_j^2(x_i) 2\sigma\left(\frac{1}{R_l} - \frac{1}{R_r}\right) \tag{10}$$

In eq 10, R_l, R_r, and σ are the left and right radii of the spherical caps, and the liquid surface tension, respectively. In the laboratory frame, the oxygen bubble moves with speed $v_b + v_j$, where v_j is the speed of the microjet (Figure 2d). The rate of change of the momentum of the subsystem bubble/tube is equal to the rate of exchange of momentum with the fluid, which is represented by the sum of the drag forces as follows:

$$\frac{d}{dt}(m_b(v_b + v_j)) + m_j\frac{dv_j}{dt} = F_{d_b} + F_{d_j} \tag{11}$$

where F_{d_b} and F_{d_j} are the drag forces on the bubble and microjet, respectively. In a low Reynolds number fluid, the inertial forces exerted on the microjet are smaller than drag forces

$$\left|m_j\frac{dv_j}{dt}\right| \ll |F_{d_j}| \tag{12}$$

Similarly, the viscous forces exerted on the bubble are dominant

$$\left|\frac{d}{dt}[m_b(v_b + v_j)]\right| \ll |F_{d_b}| \tag{13}$$

Therefore, motion of the microjet is governed by

$$F_{d_b} + F_{d_j} = 0 \tag{14}$$

The drag forces in eq 14 are given by[36]

$$F_{d_b} = 6\pi\eta r_b(v_b + v_j) \quad \text{and} \quad F_{d_j} = \frac{2\pi\eta L v_j}{\ln(L/b) + c_1} \tag{15}$$

The finite boundaries (inner surface of the microjet) exert a greater drag force on the bubble[43] than that given in eq 15. Nevertheless, we only consider the drag force at the time instant of detachment of the bubble from the microjet.[36] Therefore, we assume that the bubble is not in contact with a wall. The microjet speed is calculated based on the instantaneous equilibrium of the fluid forces as follows:

$$v_j = -\frac{3r_b v_b}{3r_b + \frac{L}{\ln(L/b) + c_1}} \tag{16}$$

where, $b = r_{max} - \frac{L}{2}\tan\phi$, and c_1 is given by[36]

$$c_1 = -\frac{1}{2} + \ln 2 - \frac{2 - \xi\tan\phi}{2\xi\tan\phi}\left[\frac{2}{2 - \xi\tan\phi}\ln\left(\frac{2}{2 - \xi\tan\phi}\right) - \frac{2 - 2\xi\tan\phi}{2 - \xi\tan\phi}\ln\left(\frac{2 - 2\xi\tan\phi}{2 - \xi\tan\phi}\right)\right] \tag{17}$$

In eq 17, $\xi = \frac{L}{r_{max}}$. The negative sign in eq 16 indicates that the microjet and the bubble are moving along opposite directions. Time-averaged microjet speed $\bar{v}_j$ is calculated from the equation given in Table 1. We begin by solving the multiple bubbles nucleation model numerically to study the influence of nucleation position, contact angle, concentration, and microjet length on unidirectional-overloaded transition in microjets.

3. SIMULATION OF MULTIPLE BUBBLES NUCLEATION MODEL

The model with multiple bubbles nucleation is applied and analyzed with the parameters summarized in Table 2.

Table 2. Simulation Parameters of the Microjet[34,40]

parameter	value	parameter	value
r [μm]	3	D_H [$m^2 \cdot s^{-1}$]	1.43×10^{-9}
r_{min} [μm]	2.5	D_0 [$m^2 \cdot s^{-1}$]	2.06×10^{-9}
r_{max} [μm]	3.5	K_H [$m \cdot s^{-1}$]	1.32×10^{-6}
L [μm]	50	K_0 [$m \cdot s^{-1}$]	5.1×10^{-4}
ϕ [°]	1.15	m_j [kg]	250×10^{-15}
c_0 [%]	1	η [Pa·s]	0.013
x_0 [μm]	10	σ [$N \cdot m^{-1}$]	0.0338

The microjet length is divided into 200 segments of length $\Delta x = 251$ nm. The time step is set to 3 μs. Influence of the bubble position on bubble shape, nucleation position x_0, contact angle θ, hydrogen peroxide concentration c_0, and microjet length L on ejected bubble radius r_e, frequency f, and microjet average speed $\bar{v}_j$ are studied using our numerical model.

A typical example of the bubble ejection from the microjet is summarized in Figure 3, at different time-laps. The time instants are 1, 20, 51, 53, 54, 58, 59, and 59.2 ms. The x-axis is parallel to the axis of the microjet, and the range from zero to microjet length (L) is represented. The microjet walls are shown using the solid black lines. On the y-axis, normalized hydrogen peroxide concentration (c_H/c_0) and normalized catalytically formed oxygen volume (V_0/V_j) are plotted using blue and red lines, respectively. At time, $t = 1$ ms, there is a small oxygen bubble at nucleation position x_0 (green circle). Small amount of oxygen is formed ($V_0/V_j \approx 0$) and small amount of hydrogen peroxide is consumed ($c_H/c_0 \approx 1$). At time $t = 20$ ms, the bubble size is increased to a radius of 1.7 μm at its initial position. Hydrogen peroxide concentration c_H/c_0 is decreased toward the center of the microjet. After time, $t = 51$ ms, the bubble size increases and its surface comes into contact with the inner wall of the microjet. At time $t = 53$ ms, the bubble obtains a conical shape, and hydrogen peroxide concentration is reduced to zero at bubble position. The bubble moves toward the wider microjet end. The hydrogen peroxide profile moves with the bubble. Simultaneously, a second bubble nucleates at position and time x_0 and 54 ms, respectively. The first bubble continues its motion and the second bubble is growing in size ($t = 58$ ms). Due to the rapid movement of the first bubble, the oxygen layer is almost zero from x_0 to L. At time, $t = 59$ ms, the first bubble reaches the

DOI: 10.1021/acs.jpcc.7b02447
J. Phys. Chem. C 2017, 121, 14854−14863

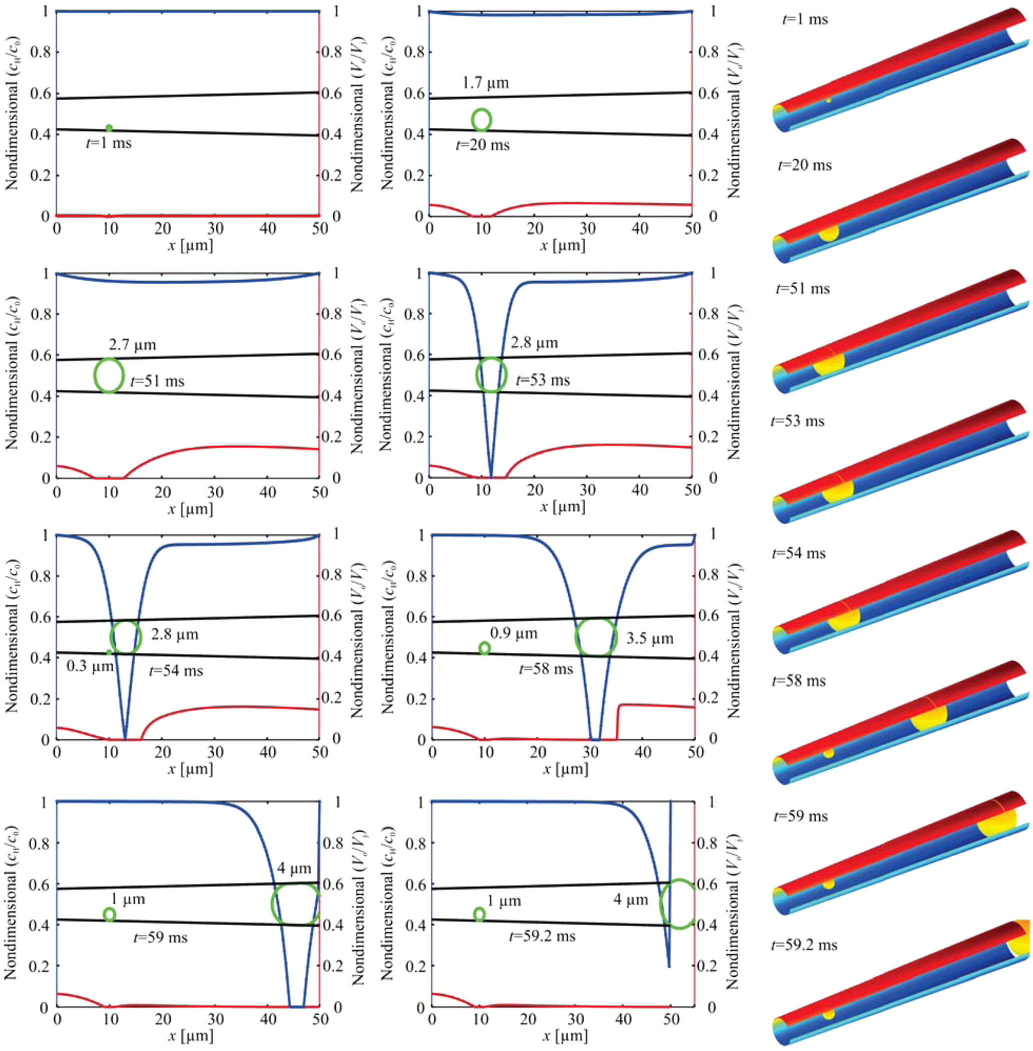

Figure 3. Simulation results for the time-resolved model with multiple bubbles formation until bubble ejection for 1 ms (top-left corner), 20 ms, 51 ms, 53 ms, 54 ms, 58 ms, 59 ms (bottom-left corner) and 59.2 ms for $x_0 = 10$ μm, $\theta = 0°$, $c_0 = 1\%$. Microjet walls (black inclined lines), oxygen bubbles (green), normalized hydrogen peroxide concentration (blue) and normalized catalytically formed oxygen volume (red). Bubbles nucleate at time, $t_1 = 0$ s and $t_2 = 54$ ms.

microjet end and is ejected at time, $t = 59.2$ ms with $r_e = 4$ μm, frequency of 16.9 Hz, and average bubble speed of 720 μm·s^{-1}. This ejection results in a unidirectional microjet movement. The bubble position $x_1(t)$ and microjet speed $v_j(t)$ are shown in Figure 4, for three periods. In the first 50.9 ms of each period, the bubble remains at its initial position and v_j is zero. Then, the bubble moves toward the wider microjet end at speed of up to 60 μm/s. The microjet moves stepwise with average speed of 200 μm/s.

It is also possible to analyze the behavior of the microjet when several bubbles are nucleated, as shown in Figure 5. At time $t = 1$ ms, two bubbles are formed at nucleation positions 10 and 40 μm. At time $t = 52$ ms, the sizes of these bubbles grow to 2.7 and 2.9 μm in radius. A third bubble is nucleated at time $t = 62$ ms, while the first and second bubbles are growing in volume and moving along the microjet. At $t = 71$ ms. Two bubbles block the microjet leading to overloaded-regime.

3.1. Influence of Nucleation Position. Bubbles have random nucleation positions in the microjet due to the inhomogeneity of the microjet surface. Figure 6 shows the

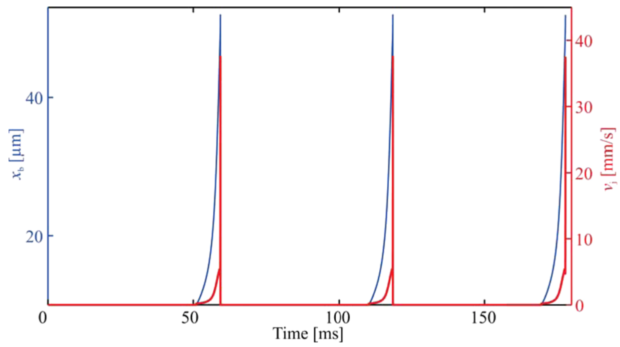

Figure 4. Bubble position $x_1(t)$ and jet speed $v_j(t)$ versus time for $x_0 = 10$ μm, $\theta = 0°$, and $c_0 = 1\%$.

influence of different nucleation positions x_0 on the speed of the microjet and the bubble ejection frequency. Unidirectional microjet movement is achieved for all nucleation positions. The maximum radius of the second bubble is 70% of the microjet radius.

DOI: 10.1021/acs.jpcc.7b02447
J. Phys. Chem. C 2017, 121, 14854−14863

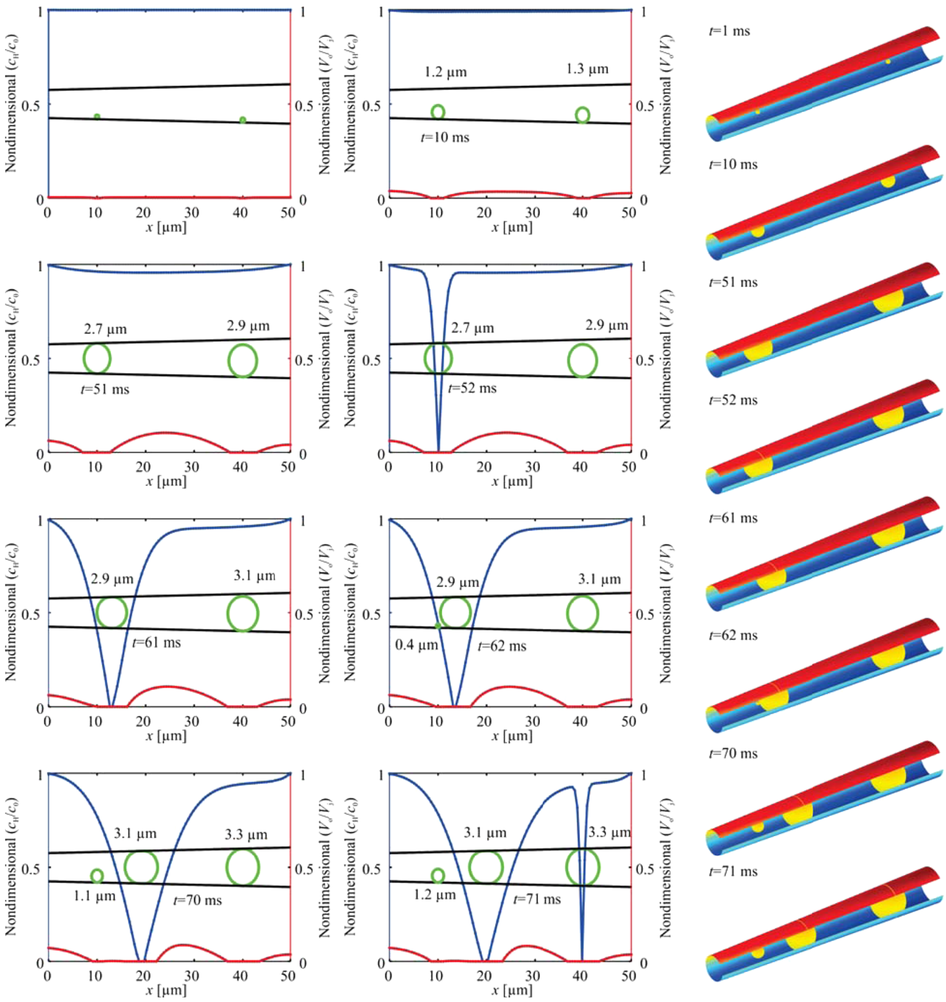

Figure 5. Simulation results for the time-resolved model with multiple bubbles (three bubbles) formation until bubble ejection for 1 ms (top-left corner), 10 ms, 51 ms, 52 ms, 61 ms, 62 ms, 70 ms (bottom-left corner), and 71 ms for x_0 = 10 and 40 μm, θ = 0°, c_0 = 1%. Microjet walls (black inclined lines), oxygen bubbles (green), normalized hydrogen peroxide concentration (blue), and normalized catalytically formed oxygen volume (red).

Ejected bubble radius, average bubble speed, and microjet speed decrease by increasing x_0, and remain constant for x_0 > 35 μm. Bubble ejection frequency of 9 to 17 Hz is achieved for relatively small and large values of x_0, respectively. As the first bubble nucleates close to the narrow microjet end, it collects a large amount of oxygen in its motion through the whole microjet. Therefore, the ejected bubble is relatively large. The bubble gains high speed toward the wide microjet end, and hence, the average speed and frequency of bubble ejection are relatively high. The second bubble has a small radius as it has short time to grow and a small surrounding from which it can collect oxygen. If the bubble nucleates close to the wide microjet end, it reaches low speed since the pressure difference is decreased. Therefore, the frequency is small, and the ejected bubble has the size of the microjet opening r_{max}. The second bubble is large as it has longer time to grow and a large surrounding to collect oxygen. These results can explain the variation of ejected bubble radius and speeds for equal microjets and conditions as the nucleation position varies randomly.

3.2. Influence of Contact Angle. We also study the influence of the contact angle on the motion of the microjet. The contact angle is varied between 0° and 13°. Representative simulation results are shown in Figure 7, for initial position,

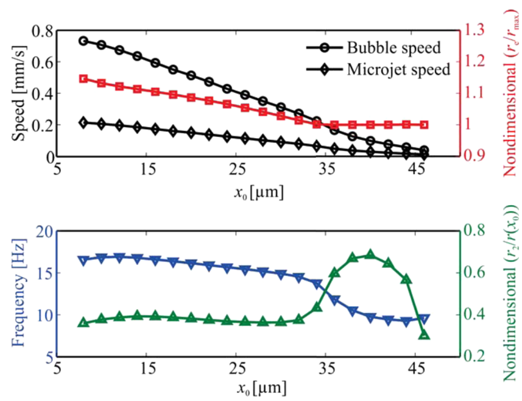

Figure 6. Dependence of average bubble speed ($\overline{v}_b$) and average jet speed ($\overline{v}_j$), normalized ejected bubble size r_e/r_{max}, frequency f and normalized second bubble radius $r_2/r_j(x_0)$ on the nucleation position x_0 for θ = 0° and c_0 = 1%.

x_0 = 10 μm and concentration of 1%. The microjet has unidirectional motion up to contact angle of 9° and the results are independent of θ. The first bubble moves at speed of 0.7 mm/s,

DOI: 10.1021/acs.jpcc.7b02447
J. Phys. Chem. C 2017, 121, 14854−14863

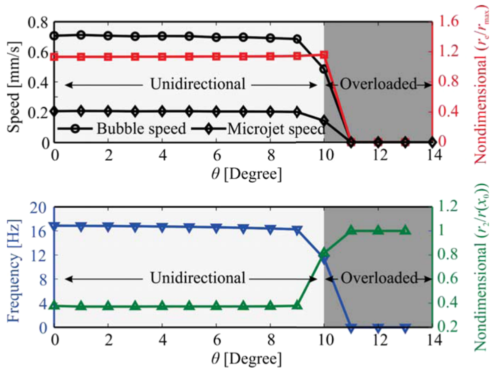

Figure 7. Dependence of average bubble and jet speeds $\bar{v}_b$ and $\bar{v}_j$, normalized ejected bubble size r_e/r_{max}, frequency f and normalized second bubble radius $r_2/r_j(x_0)$ on the contact angle θ for c_0 = 1% and x_0 = 10 μm.

and this speed results in propulsion of the microjet at speed of 200 μm/s. The bubble is ejected with radius of $1.13r_{max}$ at frequency of 17 Hz. The second bubble reaches the size of $0.37r_j$. Above 9°, the size of the second bubble increases suddenly, leading to overloaded condition, at $\theta \geq 10°$. Therefore, radius of ejected bubble, frequency, bubble speed, and microjet speed are reduced to zero. Thus, small contact angles are essential for the motion of microjets.

3.3. Influence of Concentration. More oxygen is generated at the inner surface of the microjet for relatively high hydrogen peroxide concentration based on eq 4. The microjet is overloaded above a critical concentration of 2.5% as r_2/r_j = 1. Below this critical concentration, the microjet moves unidirectionally, and bubble speed, microjet speed, radius of ejected bubble, radius of second bubble, and bubble ejection frequency increase with the concentration, as shown in Figure 8.

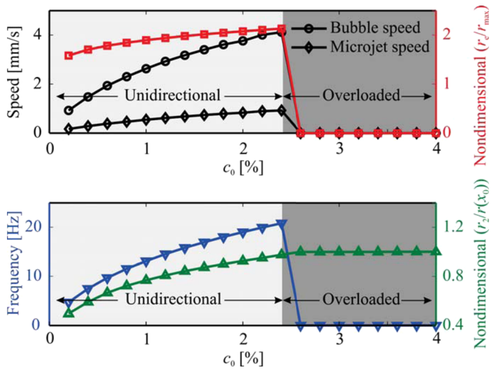

Figure 8. Dependence of average bubble speed ($\bar{v}_b$) and jet speeds ($\bar{v}_j$), normalized ejected bubble size r_e/r_{max}, frequency f and normalized second bubble radius $r_2/r_j(x_0)$ on the hydrogen peroxide concentration c_0 for θ = 0°, x_0 = 10 μm, and L = 200 μm.

The influence of the hydrogen peroxide concentration is experimentally evaluated at two representative concentrations of 1% and 5%, as shown in Figure 9. At c_H = 1%, the microjet achieves a unidirectional motion at an average speed of 108 ± 35 μm/s. This measurement is in agreement with our theoretical prediction for a range of bubble nucleation positions of $0.4L \leq x_0 \leq 0.6L$. At c_H = 5%, the microjet achieves overloaded movement, and the average speed is decreased to 22.3 ± 10.2 μm/s, as shown in Figure 9. Again, this experimental result is in qualitative agreement with our theoretical prediction. Figure 8 suggests that a transition to overloaded regime occurs for c_H > 2.5%.

3.4. Influence of Microjet Length. The influence of the length on the motion of the microjet is shown in Figure 10, for θ = 0°, x_0 = 0.1L, r = 3 μm, and ϕ = 1.14°. The microjet is overloaded above a critical length of 160 μm. Below this critical length, the microjet has a unidirectional motion. In this case, bubble speed, microjet speed, and radius of the second bubble increase linearly with the length of the microjet. The radius of ejected bubble reaches $1.4r_{max}$ at frequencies between 40 and 80 Hz.

3.5. Influence of Cone Angle. The cone angle describes the asymmetry of the microjet. In Figure 11, the influence of the cone angle ϕ on the movement of microjet is shown for the parameters given in Table 2. A transition from unidirectional to overloaded regime is observed at ϕ = 2.4°. In the unidirectional regime, bubble speed, microjet speed, and the frequency of ejection increase with the cone angle and decrease for ϕ > 2°. Maximum bubble speed, microjet speed, and frequency are 0.7 mm/s, 0.2 mm/s, and 18 Hz, respectively. On the other hand, the size of the second bubble decreases with ϕ, reaches a minimum at ϕ = 0.9°, and then increases again. The size of the ejected bubble decreases with the cone angle ϕ. These results show that the cone angle is essential to initiate microjet movement. However, the angle does not have to be accurately implemented, as there is a very broad maximum around the optimum cone angle. The cone angle for geometry in Table 2 should be in the range 1−2° to increase the speed of the microjet.

4. DISCUSSION

The multiple bubbles nucleation model resembles the bubble ejection and microjet movement. Unidirectional microjet motion is attributed to bubble ejection before microjet blockage by additional bubbles. The dependence of the results on nucleation position explains the statistical variation of behavior reported in.[15,16] The multiple bubbles nucleation model provides stepwise microjet movement similar to the experimental results in.[31] Comparison of bubble ejection frequency and microjet speed found by multiple bubbles nucleation model, experiment, growth model, and ejection model are summarized in Table 3. Our model provides a frequency smaller than the experimental frequency. However, it provides more accurate results, as opposed to other models. The microjet speed is accurately predicted by the ejection model.[32] Our model also provides the same order of magnitude as the experimental results, and overestimates the microjet speed by a factor of 2. Overloaded microjets are caused by multiple bubbles of the size of microjet radius which hinder further bubble ejection, and results in negligible displacement of the microjet. Quantitatively, overloaded microjets are found by the model for high contact angles (>10°), high hydrogen peroxide concentration (>2.5%), and relatively long microjets (>160 μm). Overloaded microjets at high contact angles can explain the experimentally reported necessary addition of surfactants to reduce contact angles.[16] The contact angle of water on platinum surface is 40°. This value is decreased by surfactants. This observation is important as the model predicts overloaded microjets above a critical angle of 9°. The predicted critical length of 160 μm (Figure 10) is in agreement with the experimental value between 150 and 200 μm.[32] Blockage of blood flow by oxygen bubbles through system of capillaries, which have similar radius and length to microjets, occurs already at 0.01−0.02 vol% hydrogen peroxide.[39] There is also good agreement between the experimental switching

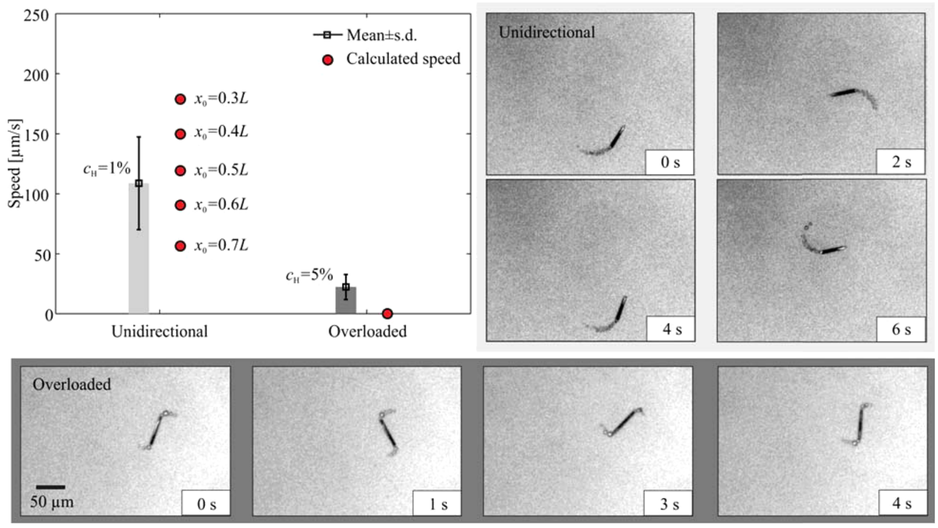

Figure 9. Calculated and measured speeds of the microjets during unidirectional and overloaded regimes. The measured speed of the microjet is 108 ± 35 μm/s during unidirectional movement for concentration of hydrogen peroxide $c_H = 1\%$, whereas the calculated speeds range between 178.7 μm/s and 56.38 μm/s for bubble nucleation position, $0.3L \leq x_0 \leq 0.7L$. The microjet achieves negligible displacement at average speed of 22.3 ± 10.2 μm/s during overloaded regime, for $c_H = 5\%$ (Supporting Movie 1 and Movie 2).

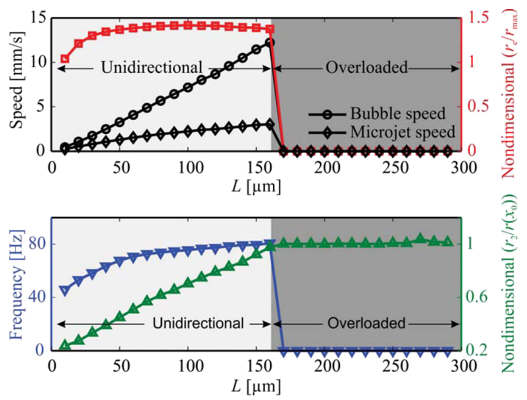

Figure 10. Dependence of average bubble speed ($\overline{v}_b$) and average jet speed ($\overline{v}_j$), normalized ejected bubble size r_e/r_{max}, frequency f and normalized second bubble radius $r_2/r_j(x_0)$ on the microjet length L for $\theta = 0°$, $x_0 = 0.1L$, $r = 3$ μm, $c_0 = 7\%$, and $\phi = 1.14°$.

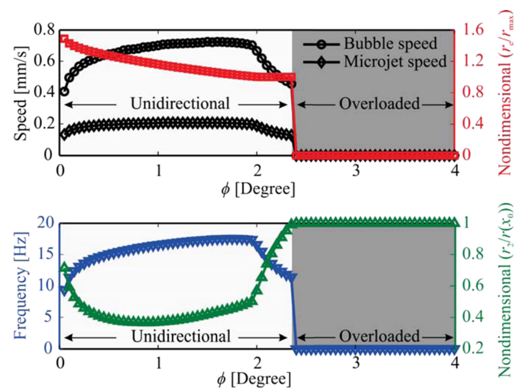

Figure 11. Dependence of average bubble speed ($\overline{v}_b$) and average jet speed ($\overline{v}_j$), normalized ejected bubble size r_e/r_{max}, frequency f, and normalized second bubble radius $r_2/r_j(x_0)$ on the cone angle ϕ of the microjet for $\theta = 0°$, $x_0 = 0.1L$, $r = 3$ μm, and $c_0 = 7\%$.

Table 3. Experimental and Theoretical Ejection Frequency (f) and Average Microjet Speed ($\overline{v}_j$) Determined for Hydrogen Peroxide Concentration c_H = 1%, Viscosity η = 1.13 mPa·s, Tube Length L = 50 μm, Tube Radius r_j = 3 μm, Tube Mass m_j = 250 pg, and Bubble Nucleation Point x_0 = L/5

model	f [Hz]	$\overline{v}_j$ [μm/s]
experiment[34]	30	100
ejection model[32]	1.43	70
growth model[31]	0.035	≈0
multiple bubbles nucleation model (current study)	17	200

to overloaded condition for large concentrations and high microjet lengths, which expands currently existing models for unidirectional movement.

5. CONCLUSIONS

We present a model with multiple bubbles nucleation that describes the locomotion of microjets. Multiple bubbles are introduced to differentiate between unidirectional and overloaded microjet movement. This model addresses the overloaded microjet behavior and predicts a transition between unidirectional and overloaded microjet movement for high contact angles, high concentration of hydrogen peroxide solution, and relatively long microjets. Furthermore, quantitative agreement with experimental limits of unidirectional behavior is found with values of contact angles of approximately 10°, hydrogen peroxide concentration of approximately 2.5%, and microjet length of 160 μm. The multiple bubbles nucleation model provides values comparable to experiments, as shown in Table 3. As part of future studies, the model will be extended for more than one bubble ejection to find the influence of residual oxygen. In addition, we will use the multiple bubbles nucleation model to optimize the design of microjets.

■ ASSOCIATED CONTENT

Supporting Information

The Supporting Information is available free of charge on the ACS Publications website at DOI: 10.1021/acs.jpcc.7b02447.

DOI: 10.1021/acs.jpcc.7b02447
J. Phys. Chem. C 2017, 121, 14854−14863

Microjet during unidirectional regime (AVI)
Microjet during overloaded regime (AVI)

Corresponding Authors
*E-mail: islam.shoukry@guc.edu.eg.

■ AUTHOR INFORMATION

ORCID
Islam S. M. Khalil: 0000-0003-0617-088X

Notes
The authors declare no competing financial interest.

■ ACKNOWLEDGMENTS

The research leading to these results has received funding from the German University in Cairo and the DAAD-BMBF funding project. The authors also acknowledge the funding from the Science and Technology Development Fund in Egypt (No. 23016).

■ REFERENCES

(1) Ghosh, A.; Fischer, P. Controlled Propulsion of Artificial Magnetic Nanostructured Propellers. *Nano Lett.* **2009**, *9*, 2243−2245.
(2) Dreyfus, R.; Baudry, J.; Roper, M. L.; Fermigier, M.; Stone, H. A.; Bibette, J. Microscopic Artificial Swimmers. *Nature* **2005**, *437*, 862−865.
(3) Peyer, K. E.; Zhang, L.; Nelson, B. J. 'Bio-Inspired Magnetic Swimming Microrobots for Biomedical Applications. *Nanoscale* **2013**, *5*, 1259−1272.
(4) Khalil, I. S. M.; Dijkslag, H. C.; Abelmann, L.; Misra, S. MagnetoSperm: A Microrobot that Navigates using Weak Magnetic Fields. *Appl. Phys. Lett.* **2014**, *104*, 223701.
(5) Magdanz, V.; Sanchez, S.; Schmidt, O. G. Development of a Sperm-Flagella Driven Micro-Bio-Robot. *Adv. Mater.* **2013**, *25*, 6581−6588.
(6) Khalil, I. S. M.; Tabak, A. F.; Klingner, A.; Sitti, M. Magnetic Propulsion of Robotic Sperms at Low-Reynolds Number. *Appl. Phys. Lett.* **2016**, *109*, 033701.
(7) Zhuang, J.; Carlsen, R. W.; Sitti, M. pH-Taxis of Biohybrid Microsystems. *Sci. Rep.* **2015**, *5*, 11403.
(8) Wang, J.; Gao, W. Nano/Microscale Motors: Biomedical Opportunities and Challenges. *ACS Nano* **2012**, *6*, 5745−5751.
(9) Nelson, B. J.; Kaliakatsos, I. K.; Abbott, J. J. Microrobots for Minimally Invasive Medicine. *Annu. Rev. Biomed. Eng.* **2010**, *12*, 55−85.
(10) Servant, A.; Qiu, F.; Mazza, M.; Kostarelos, K.; Nelson, B. J. Controlled In Vivo Swimming of a Swarm of Bacteria-Like Microrobotic Flagella. *Adv. Mater.* **2015**, *27*, 2981−2988.
(11) Srivastava, S. K.; Medina-Sánchez, M.; Koch, B.; Schmidt, O. G. Medibots: Dual-Action Biogenic Microdaggers for Single-Cell Surgery and Drug Release. *Adv. Mater.* **2016**, *28*, 832−837.
(12) Paxton, W. F.; Kistler, K. C.; Olmeda, C. C.; Sen, A.; St. Angelo, S. K.; Cao, Y.; Mallouk, T. E.; Lammert, P. E.; Crespi, V. H. Catalytic Nanomotors: Autonomous Movement of Striped Nanorods. *J. Am. Chem. Soc.* **2004**, *126*, 13424−13431.
(13) Fournier-Bidoz, S.; Arsenault, A. C.; Manners, I.; Ozin, G. A. Synthetic Self-Propelled Nanorotors. *Chem. Commun. (Cambridge, U. K.)* **2005**, *4*, 441−443.
(14) Howse, J. R.; Jones, R. A. L.; Ryan, A. J.; Gough, T.; Vafabakhsh, R.; Golestanian, R. Self-Motile Colloidal Particles: From Directed Propulsion to Random Walk. *Phys. Rev. Lett.* **2007**, *99*, 048102.
(15) Mei, Y. F.; Huang, G.; Solovev, A. A.; Urena, E. B.; Monch, I.; Ding, F.; Reindl, T.; Fu, R. K. Y.; Chu, P. K.; Schmidt, O. G. Versatile Approach for Integrative and Functionalized Tubes by Strain Engineering of Nanomembranes on Polymers. *Adv. Mater.* **2008**, *20*, 4085−4090.
(16) Solovev, A. A.; Mei, Y. F.; Urena, E. B.; Huang, G.; Schmidt, O. G. Catalytic Microtubular Jet Engines Self-Propelled by Accumulated Gas Bubbles. *Small* **2009**, *5*, 1688−1692.
(17) Gao, W.; D'Agostino, M.; Garcia-Gradilla, V.; Orozco, J.; Wang, J. Multi-Fuel Driven Janus Micromotors. *Small* **2013**, *9*, 467−471.
(18) Gao, W.; Pei, A.; Wang, J. Water-Driven Micromotors. *ACS Nano* **2012**, *6*, 8432−8438.
(19) Wang, Y.; Hernandez, R. M.; Bartlett, D. J., Jr.; Bingham, J. M.; Kline, T. R.; Sen, A.; Mallouk, T. E. Bipolar Electrochemical Mechanism for the Propulsion of Catalytic Nanomotors in Hydrogen Peroxide Solutions. *Langmuir* **2006**, *22*, 10451−10456.
(20) Torrejon, J.; Badini-Confalonieri, G.; Vazquez, M. Fabrication and Magnetic Properties of Hard/Soft Magnetostatically Coupled Fe Pt/Fe Ni Multilayer Microwires. *J. Appl. Phys.* **2008**, *103*, 07E712.
(21) Youakim, K.; Ehab, M.; Hatem, O.; Misra, S.; Khalil, I. S. M. Paramagnetic Microparticles Sliding on a Surface: Characterization and Closed-Loop Motion Control. *Proceedings of the IEEE International Conference on Robotics and Automation*, Seattle, WA, May 2015, 4068−4073.
(22) Zhang, L.; Abbott, J. J.; Dong, L.; Kratochvil, B. E.; Bell, D.; Nelson, B. J. Artificial Bacterial Flagella: Fabrication and Magnetic Control. *Appl. Phys. Lett.* **2009**, *94*, 064107.
(23) Khalil, I. S. M.; Youakim, K.; Sánchez, A.; Misra, S. Magnetic-Based Motion Control of Sperm-Shaped Microrobots using Weak Oscillating Magnetic Fields. *Proceedings of the IEEE International Conference of Robotics and Systems*, Chicago, IL, Sep. 2014, 4686−4691.
(24) Solovev, A. A. Catalytic tubular microjet engines. Ph.D. Thesis, TU Chemnitz, IFW Dresden, 2012.
(25) Khalil, I. S. M.; Magdanz, V.; Sanchez, S. O.; Schmidt, O. G.; Misra, S. Wireless Magnetic-Based Closed-Loop Control of Self-Propelled Microjets. *PLoS One* **2014**, *9*, e83053.
(26) Khalil, I. S. M.; Magdanz, V.; Sanchez, S.; Schmidt, O. G.; Misra, S. Three-Dimensional Closed-Loop Control of Self-Propelled Microjets. *Appl. Phys. Lett.* **2013**, *103*, 172404.
(27) Manjare, M.; Yang, B.; Zhao, Y.-P. Bubble Driven Quasioscillatory Translational Motion of Catalytic Micromotors. *Phys. Rev. Lett.* **2012**, *109*, 128305.
(28) Huang, G.; Mei, Y.; Cavallo, F.; Baunack, S.; Coric, E.; Gemming, T.; Bertram, F.; Christen, J.; Fu, R. K. Y.; Chu, P. K.; Schmidt, O. G. Fabrication and Optical Properties of C/β -SiC/Si hybrid rolled-up microtubes. *J. Appl. Phys.* **2009**, *105*, 016103.
(29) Gao, W.; Sattayasamitsathit, S.; Wang, J. Catalytically Propelled Micro-/Nanomotors: How Fast Can They Move? *Chem. Rec.* **2012**, *12*, 224−231.
(30) Favelukis, M.; Yablonsky, G. S. Catalytic Bubble Model: Bubble Growth with an Interfacial Chemical Reaction. *Ind. Eng. Chem. Res.* **2004**, *43*, 4476−4482.
(31) Manjare, M.; Yang, B.; Zhao, Y.-P. Bubble-Propelled Microjets: Model and Experiment. *J. Phys. Chem. C* **2013**, *117*, 4657−4665.
(32) Li, J.; Huang, G.; Ye, M.; Li, M.; Liu, R.; Mei, Y. Dynamics of Catalytic Tubular Microjet Engines: Dependence on Geometry and Chemical Environment. *Nanoscale* **2011**, *3*, 5083−5089.
(33) Li, L.; Wang, J.; Li, T.; Song, W.; Zhang, G. Hydrodynamics and Propulsion Mechanism of Self-Propelled Catalytic Micromotors: Model and Experiment. *Soft Matter* **2014**, *10*, 7511−7518.
(34) Fomin, V. M.; Hippler, M.; Magdanz, V.; Sanchez, S.; Schmidt, O. G. Propulsion Mechanism of Catalytic Microjet Engines. *IEEE Transactions on Robotics* **2014**, *30*, 40−48.
(35) Wang, H.; Zhao, G.; Pumera, M. Crucial Role of Surfactants in Bubble-Propelled Microengines. *J. Phys. Chem. C* **2014**, *118*, 5268−5274.
(36) Li, L.; Wang, J.; Li, T.; Song, W.; Zhang, G. A Unified Model of Drag Force for Bubble-Propelled Catalytic Micro/Nano-Motors with Different Geometries in Low Reynolds Number Flows. *J. Appl. Phys.* **2015**, *117*, 104308.
(37) Sarkis, B.; Folio, D.; Ferreira, A. Catalytic Tubular Microjet Propulsion Model for Endovascular Navigation. *Proceedings of the IEEE International conference on robotics and automation (ICRA)*, Seattle, WA, May 2015, 3537−3542.
(38) Giulivi, C.; Hochstein, P.; Davies, K. J. Hydrogen Peroxide Production by Red Blood Cells. *Free Radical Biol. Med.* **1994**, *16*, 123−129.

DOI: 10.1021/acs.jpcc.7b02447
J. Phys. Chem. C 2017, 121, 14854−14863

(39) Johnson, R. J. R.; Froese, G.; Khodadad, M.; Gibson, D. Hydrogen Peroxide and Radiotherapy. Bubble Formation in Blood. *Br. J. Radiol.* **1968**, *41*, 749−754.

(40) Vanstroebiezen, S. A. M.; Everaerts, F. M.; Janssen, L. J. J.; Tacken, R. A. Diffusion-Coefficients of Oxygen, Hydrogen-Peroxide and Glucose in a Hydrogel. *Anal. Chim. Acta* **1993**, *273*, 553−560.

(41) Jensen, M. J. Bubbles in Microchannels. M.Sc. Dissertation, Technical University of Denmark, 2002.

(42) Clanet, C.; Hèraud, P.; Searby, G. On the Motion of Bubbles in Vertical Tubes of Arbitrary Cross-Sections: Some Complements to the Dumitrescu-Taylor Problem. *J. Fluid Mech.* **1999**, *519*, 359−376.

(43) Ataíde, C. H.; Pereira, F. A. R.; Barrozo, M. A. S. Wall Effects on the Terminal Velocity of Spherical Particles in Newtonian and Non-Newtonian Fluids. *Braz. J. Chem. Eng.* **1999**, *16*, 387.

DOI: 10.1021/acs.jpcc.7b02447
J. Phys. Chem. C 2017, 121, 14854−14863